

# INVESTIGATION OF FOUR VORTEX SYSTEM WAKE CHARACTERISTICS

A. Allen, C. Breitsamter

Technische Universität München (TUM), Lehrstuhl für Aerodynamik (AER)  
Boltzmannstrasse 15, 85748 Garching  
Germany

## OVERVIEW

An experimental investigation on the wake vortex formation and evolution of a four vortex system of a generic model in the near field and extended near field as well as the behaviour and decay in the far field region has been conducted by means of hot-wire anemometry in a wind tunnel. The results were obtained during an experimental campaign as part of the EC project FAR-Wake. The model used consists of a wing-tail plane configuration with the wing producing positive lift and the tail plane negative lift. The circulation ratio of tail to wing is  $-0.3$  and the span ratio is  $0.3$ . Thus, a four vortex system with counter-rotating neighboured vortices exists. The model set-up was chosen on the condition to create a most promising four vortex system with respect to accelerate wake vortex decay by optimal perturbations enhancing inherent instability mechanisms. The flow field has been investigated up to a distance of 48 span dimensions downstream of the model and the results obtained at 1, 12, 24 and 48 span distances are shown as non-dimensional axial vorticity and vertical turbulence intensities. A significant decay in peak vorticity is observable during the downward motion of the vortices. Spectral analysis of the unsteady velocity data reveals a peak in the power spectral density distributions indicating the presence of a dominating instability. Cross spectral density distributions have also been extracted from the data gathered from two hot-wire probes, which highlight the co-operative instability leading to a rapid wake vortex decay within 30 span dimensions downstream.

## NOMENCLATURE

$AR$	aspect ratio
$b$	span
$b_0$	lateral distance of main vortex pair
$b_M$	distance between two main vortices
$c$	chord length
$C_L$	lift coefficient
$d$	distance between the two adjacent vortices of a four vortex system
$f$	frequency
$F$	area
$k$	reduced frequency
$R_b$	span ratio

$R_\Gamma$	circulation ratio
$Re_c$	Reynolds number based on the wing chord length
$S_{u'}^N$	non-dimensional power spectral density of $u'$
$S_{c,v'}^N$	non-dimensional cross spectral density of $v'$
$Tu_z$	vertical turbulence intensity
$u, v, w$	axial, lateral and vertical velocities
$\bar{u}, \bar{v}, \bar{w}$	mean axial, lateral and vertical velocities
$u', v', w'$	fluctuation part of $u, v$ and $w$
$U_\infty$	free stream velocity
$x, y, z$	coordinates in $x$ -, $y$ - and $z$ -direction
$x^*, y^*, z^*$	non-dimensional coordinates in $x$ -, $y$ - and $z$ -direction
$\alpha$	angle of attack
$\eta_{HTP}$	horizontal tail plane setting
$\Gamma$	circulation
$\lambda$	wavelength
$\tau^*$	non-dimensional time
$\xi$	non-dimensional axial vorticity
<i>Subscripts</i>	
dom	dominant
HTP	horizontal tail plane
W	wing

## 1 INTRODUCTION

Trailing vortices of Large Transport Aircraft are a potential threat to succeeding aircraft encountering the wake.<sup>1,2</sup> This is especially dangerous, when the aircraft are at take-off and landing. The following aircraft may experience a sudden decrease of climb rate or even rapid descent, a rolling motion or an overload of the aircraft's structure. In order to avoid a dangerous impact of these vortices, minimum separation distances for cruise, approach and take-off were established. To increase the number of aircraft capable of landing at an airport within a given time period, the wake vortex strength should decay within a smaller distance than the separation distance is at the moment. At the Institute of Aerodynamics (AER) of the Technische Universität München (TUM) a wind tunnel investigation is conducted within the framework of the EU funded project "Fundamental Research on Aircraft Wake Phenomena" (FAR-Wake) on a generic

model generating a four vortex system.

Precise prediction of wake vortex trajectories and decay under all weather conditions is beyond the range of current technology. Therefore, many research activities concentrate on alleviating the wake vortex hazard by modifications of wing geometry and/or wing loading.<sup>3</sup> Strategies to minimise the wake vortex hazard concentrate either on a Quickly Decaying Vortex (QDV) or on a Low Vorticity Vortex (LVV) design. An enhanced vortex decay (QDV) may be achieved by promoting three-dimensional instabilities by means of active or passive devices. An active system tested by Boeing uses periodically oscillating control surfaces to introduce the desired perturbations leading, after sufficient amplification, to the break-up of the vortices.<sup>4</sup> The LVV design reduces the wake vortex hazard by enhancing the diffusion of the vorticity field. It is aimed on the generation of wake vortices with larger core size and smaller swirl velocities at the core radius after roll-up is completed. This may be achieved by injecting additional turbulence into the wake to increase the dispersion of vorticity and/or by altering the circulation distribution of the wake generating wing. The first type of mechanism is related to the use of spoilers or wing fins while the second type of mechanism is related e.g. to differential flap setting.<sup>5</sup>

With respect to 3D perturbations vortex systems are generally unstable. The related mechanisms are summarized in a FAR-Wake position paper.<sup>6</sup> Instabilities are caused by the amplification of asymmetric Kelvin waves under mutual straining of the vortices. If the separation between the vortices is large in comparison to their diameter, a system of stability equations can be derived by considering parallel vortex filaments with slight sinusoidal perturbations of their respective position. The equations of this linear system are given by Crow<sup>7</sup> for two counter-rotating vortices and by Crouch<sup>8</sup> and Fabre et al.<sup>9,10</sup> for multiple vortex pairs. The system evolves due to the superposition of three effects: a) the straining experienced by each filament when displaced by a perturbation from its mean position in the velocity field induced by the other undisturbed filaments, b) the self induced rotation of the disturbed filament c) the velocity field induced on the filament by the other vortices when perturbed from their mean positions.<sup>7</sup> The mechanism which strains the vortex due to the displacement from its mean position in the velocity field by a perturbation induced by the other vortex filaments leads (mechanism a) to an amplification of the asymmetric Kelvin waves in case their polarization planes remain close to the extension planes of the straining field. This mechanism is balanced with the self induced rotation (mechanism b) which tends to shift the perturbation away from these planes. The frequency of this self induced oscillation is the frequency of the oscillation mode of the Kelvin displacement wave.<sup>9</sup> This mechanism introduces a dependence of the solution with respect to a measure of the

diameter of the vortex core. Long wave co-operative instabilities are of prime importance for applications to aircraft hazard alleviation as it could be possible that the dispersion of a vortex wake might be accelerated by means of this mechanism.

Especially the stability properties of a vortex configuration composed of two counter-rotating vortex pairs have been considered. The vortex pairs can be co-rotating ( $\Gamma_1 > 0, \Gamma_2 < 0$ ) or counter-rotating ( $\Gamma_1 > 0, \Gamma_2 < 0$ ).<sup>11</sup> In the wake of an aircraft, the outer vortex pair is produced at the wing tips or outer flap edges and the inner one by the inner flap edges or the horizontal tail plane. The linear stability method described above can be applied, whereby the solution depends on  $R_\Gamma = \Gamma_2/\Gamma_1$  and  $R_b = b_2/b_1$ . Without inner vortices the classical Crow instability develops on the outer vortex pair. Adding the second vortex pair leads to much higher amplifications.<sup>9,10</sup> The initially introduced perturbation has been amplified by nearly a factor of 6000 after one revolution of the inner vortices around the outer vortex pair. This amplification must be compared to the value obtained for the Crow instability (2.2) without the inner vortex pair. A towing tank result ( $R_\Gamma = -0.37; R_b = 0.5$ ) confirms that this type of perturbation is effectively selected in a real four vortex wake.<sup>12,13</sup>

## 2 EXPERIMENTAL SET-UP

### 2.1 Model

The wind tunnel model used is the DLR F13 model, which is a full model depicted in Fig. 1. It consists of a cambered wing ( $b_W = 0.3 \text{ m}; c_W = 0.05 \text{ m}; F_W = 0.015 \text{ m}^2; AR_W = 6.0$ ), which has a fixed angle of attack of  $\alpha = 10^\circ$  and a horizontal tail plane ( $b_{HTP} = 0.09 \text{ m}; c_{HTP} = 0.035 \text{ m}; F_{HTP} = 0.00315 \text{ m}^2; AR_{HTP} = 2.57$ ), which is inclined at  $-4^\circ$ . The ratio of the spans of the wing and the horizontal



Figure 1: The DLR F13 model in wind tunnel facility C at TUM-AER

tail plane is  $R_b = 0.3$ . The ratio of the circulation of the two trailing vortex pairs emanating from the wing and the horizontal tail plane is set to  $R_\Gamma = -0.3$  to meet the requirements for optimal perturbations developing on the main vortex pair based on linear stability analysis. The circulation ratio has been determined by force measurements, see Sec 3.1. The flow field behind the model is carefully investigated at a Reynolds number of  $Re_c = 8 \cdot 10^4$ .

The coordinate system for the model is a right hand system with  $x$  in free stream direction,  $y$  in span wise direction to the right and  $z$  in vertical direction upwards. The results will be plotted in non-dimensional coordinates  $x^* = x/b$ ,  $y^* = 2y/b$  and  $z^* = 2z/b$ .

## 2.2 Wind tunnel

The wind tunnel facility C of the Institute of Aerodynamics of the Technische Universität München has a closed test section of  $21\text{ m} \times 2.7\text{ m} \times 1.8\text{ m}$  (length  $\times$  width  $\times$  height) as shown in Fig. 2. The length of the tunnel test section allows an investigation of the wake vortex system at several cross-flow planes up to 48 span dimensions downstream of the model.

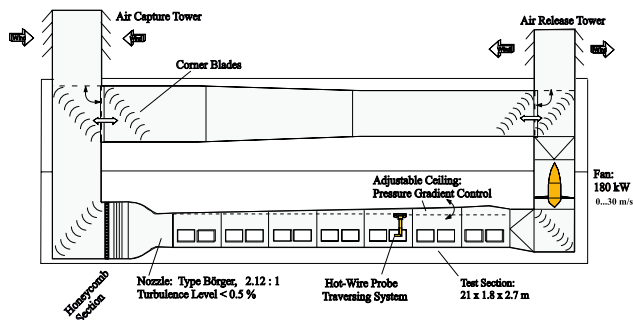


Figure 2: The wind tunnel facility C at TUM-AER

## 2.3 Hot-wire anemometry

The time dependent velocity data gathered by hot-wire anemometry using a triple sensor probe is used to calculate the mean velocity and the vorticity as well as to perform an analysis of the turbulent flow field and a spectral analysis.<sup>16</sup> The amplification of instability mechanisms of a four vortex system with counter-rotating outboard and inboard vortices will be shown.<sup>3,14,15</sup> The hot wire probe operated by a multi-channel constant temperature anemometer system was positioned downstream of the model and the velocities  $u$ ,  $v$  and  $w$  have been measured at a sampling rate of  $f_M = 3000\text{ Hz}$  (Nyquist frequency  $1500\text{ Hz}$ ) for  $6.4\text{ s}$ . The tungsten wires of the probe are platinum plated and have a diameter of  $5\mu\text{m}$  and a length of approximately  $1.25\text{ mm}$ . The sampling time corresponds to 19200 values per wire and survey point. The voltages of the hot-wire anemometer are low-pass filtered

at  $1000\text{ Hz}$  and digitized with 16 bit precision. The anemometer output signals are converted into time dependent velocity components  $u$ ,  $v$  and  $w$  using a look-up table previously obtained from the velocity and angle dependent calibration of the hot-wire probe.

## 2.4 Test conditions and data reduction

The free stream velocity  $U_\infty$  is  $25\text{ m/s}$  which corresponds to a Reynolds number of approx.  $8 \cdot 10^4$  based on the wing chord length. The velocity data is then used to calculate the vorticity and the turbulence intensities using the equations stated below. The symbol  $\xi$  denotes the non-dimensional axial vorticity and  $Tu_z$  the root mean square value of the vertical velocity fluctuations normalized with the free stream velocity.

$$(1) \quad \xi = \frac{b/2}{U_\infty} \left( \frac{\partial \bar{w}}{\partial y} - \frac{\partial \bar{v}}{\partial z} \right)$$

$$(2) \quad Tu_z = \frac{\sqrt{\overline{w'^2}}}{U_\infty}$$

Power spectral density distributions of the axial velocity fluctuations are evaluated to detect spectral peaks associated with inherent instability mechanisms. The spectral densities are calculated using a Fast Fourier Transformation (FFT) of the velocity fluctuation time series with a linear band averaging based on  $n_f = 1024$  frequency bands.  $S_{u'}^N$  denotes the power spectral density of  $u'$  normalized with the free stream velocity, the variance of  $u'$  and the wing span.

$$(3) \quad S_{u'}^N = S_{u'} \frac{\Delta k U_\infty}{u'^2 (b/2)}; \quad \Delta k = \frac{f_M (b/2)}{2n_f U_\infty}$$

The cross spectral density is normalized in the same way.

## 3 RESULTS

### 3.1 Force measurement

The force measurements have been conducted using a six component balance. Fig. 3 shows the curves for the circulation ratio of wing and tail plane  $R_\Gamma$ , calculated according to Eq. 4, as function of the horizontal tail plane setting  $\eta_{HTP}$  for three Reynolds numbers.

$$(4) \quad R_\Gamma = \frac{\Gamma_{HTP}}{\Gamma_W} = \frac{C_{L,HTP}}{C_{L,W}} \frac{F_W}{F_{HTP}}$$

The required circulation ratio  $R_\Gamma = -0.3$  is reached for  $\eta_{HTP} = -4.0^\circ$ . The corresponding lift coefficient for  $Re_c = 8 \cdot 10^4$  is  $C_L = 1.04$ .

The flow field measurements have only been performed at the lowest Reynolds number  $Re_c = 8 \times 10^4$ .

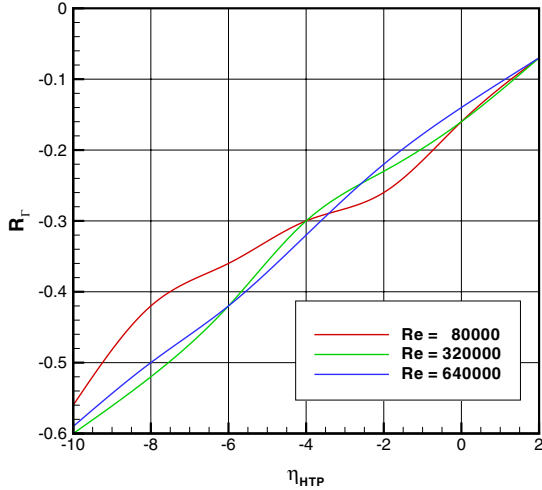


Figure 3: Circulation ratio over HTP deflection

### 3.2 Flow field measurements

The flow field has been investigated at discrete planes perpendicular to the free stream flow direction at  $x^* = x/b = 1.0, 4.0, 8.0, 12.0, 16.0, 20.0, 24.0, 36.0$  and  $48.0$ . Only four of these planes ( $x^* = 1.0, 12.0, 24.0, 48.0$ ) will be discussed here. The downstream stations are marked by the non-dimensional distance  $x^*$  and the characteristic time  $\tau^*$ . The latter number is based on an elliptical lift distribution taking into account aspect ratio and lift coefficient as stated in Eq. 5.

$$(5) \quad \tau^* = \frac{x^* 16 C_L}{\pi^4 A R}$$

For each plane the non-dimensional axial vorticity  $\xi$  and vertical turbulence intensity  $Tu_z$  are plotted. Figs. 4 and 7 show the quantities for  $x^* = 1.0$  ( $\tau^* = 0.029$ ). Note, that vorticity levels between  $-1$  and  $1$  are blanked in Fig. 4. The WTV is clearly visible at  $(y^*; z^*)_{WTV} = (0.977; -0.100)$  being the vortex with the highest peak vorticity ( $33.5$ ) and rotating counter-clockwise. At  $(y^*; z^*)_{HTV} = (0.270; -0.035)$  the HTV is visible rotating clockwise with a peak vorticity of  $(-21.1)$ . The relatively small difference in the peak values is due to the position of the measuring plane being only  $0.22 b$  downstream of the HTP trailing edge, but one span downstream of the wing trailing edge. At the top left of the HTV the vortex sheet of the HTP is still visible as it is not yet fully rolled up into the HTV. At the left upper edge of the measurement plane two weaker vortices are visible at  $(y^*; z^*) = (0.066; 0.200)$  and  $(y^*; z^*) = (0.014; 0.021)$  turning clockwise and counter-clockwise, respectively. These vortices are caused by the change in circulation through the fuselage interacting with the lifting surfaces, i.e. with the wing and the HTP. The drop in circulation in the fuselage area of a lifting surface creates a counter-rotating vortex in comparison to the tip vortex of the lifting surface. The position of the

lower of the two weak vortices in comparison to the remainder of the shear layer of the HTP and the direction of rotation indicate that this vortex is caused by the HTP, whereas the upper one is then assigned to the wing-fuselage interaction.

Fig. 7 displays the turbulence distribution in vertical direction for this measuring plane. Note, that values below  $0.02$  are blanked for all turbulence intensity images for all measuring positions. High turbulence intensities can be found at the vortex core positions and the shear layer emanating from the wing can be seen at the lower part of the measuring plane. The roll up of the shear layer into the WTV is almost complete as there is only little contact between the turbulence in the vortex and the shear layer.

The next measuring plane downstream is at  $x^* = 12.0$  ( $\tau^* = 0.342$ ), the results of which are shown in Figs. 5 and 8. In the vorticity distribution values between  $-0.1$  and  $0.1$  are blanked. A clear vorticity peak of  $7.7$  can be found at  $(y^*; z^*)_{WTV} = (1.06; -0.747)$  for the WTV. The peak vorticity for the HTV is only  $-0.5$  at  $(y^*; z^*)_{HTV} = (0.293; -0.520)$ . These positions indicate a downward and outward movement of both vortices. The peak vorticity for the HTV is difficult to find as the area of vorticity of this magnitude is quite large. Both vortices clearly show speckles at their boundaries, indicating that vorticity is spread over a quite large spatial area. The turbulence intensity again shows increased values for the position of the WTV.

Figs. 6 and 9 illustrate the results obtained at  $x^* = 24.0$  ( $\tau^* = 0.683$ ). The WTV can still be seen at  $(y^*; z^*)_{WTV} = (1.17; -1.290)$  with a vorticity peak of  $2.53$ . Note that vorticity levels between  $-0.1$  and  $0.1$  are again blanked. This mean position indicates a continuing downward and outward motion of the WTV. The main vortex clearly shows a very large spatial area of vorticity spots. Due to a strong interaction between main (outer) vortex (WTV) and secondary (inner) vortex (WTV) vorticity of the main vortex is radially spread out decreasing strongly the peak vorticity level. Thus, the vortex induced velocities are also markedly reduced which results in a significantly lower induced rolling moment on a follower aircraft. At this downstream measuring position the location of the HTV could not be determined, as the vorticity drops so low, that a clear peak is not determinable. The higher turbulence levels are confined to the WTV, which have slightly decreased.

At  $x^* = 48.0$  ( $\tau^* = 1.367$ ) the position and rotational direction of the WTV is difficult to extract, Figs. 10 and 11. The HTV is not visible in the vorticity distribution any more whereas the WTV is visible at  $(y^*; z^*)_{WTV} = (1.35; -1.930)$  with a peak vorticity of  $0.35$ . Values between  $-0.05$  and  $0.05$  are blanked. The spatial area of distributed vorticity has nearly doubled in comparison to  $x^* = 24.0$  while the peak vorticity level has decreased by approx.  $90\%$ . This vorticity distribution reflects the dissolution of the initially con-

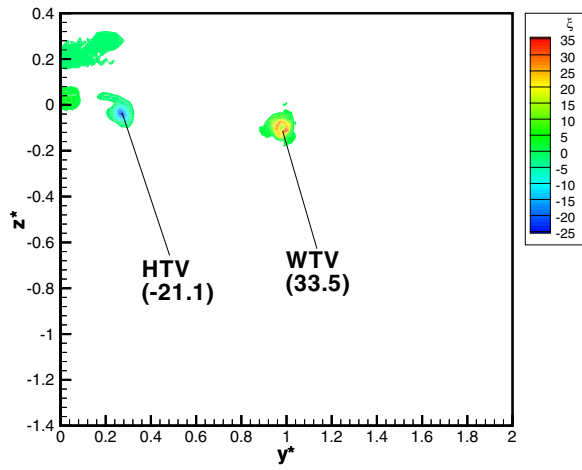


Figure 4: Contour plot of non-dimensional axial vorticity  $\xi$  at  $x^* = 1.0$  and  $Re_c = 8 \times 10^4$

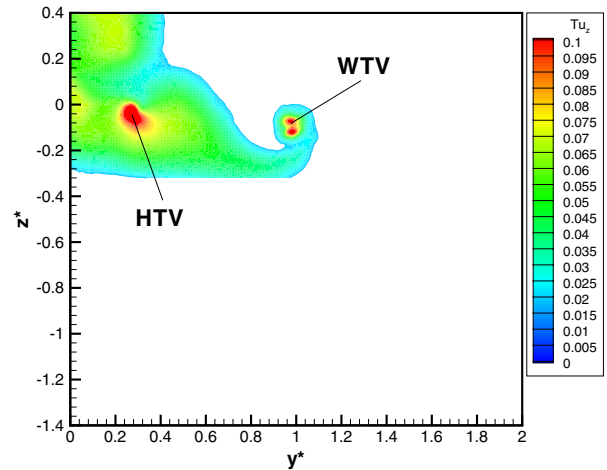


Figure 7: Contour plot of turbulence intensity  $Tu_z$  at  $x^* = 1.0$  and  $Re_c = 8 \times 10^4$

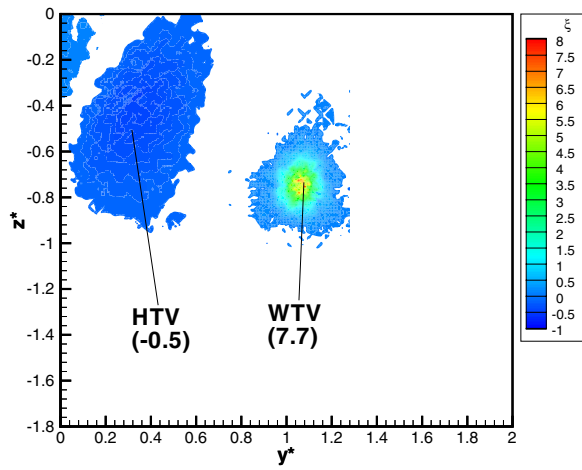


Figure 5: Contour plot of non-dimensional axial vorticity  $\xi$  at  $x^* = 12.0$  and  $Re_c = 8 \times 10^4$

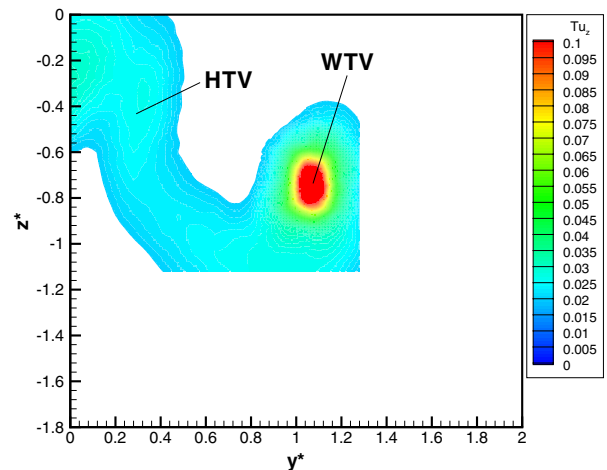


Figure 8: Contour plot of turbulence intensity  $Tu_z$  at  $x^* = 12.0$  and  $Re_c = 8 \times 10^4$

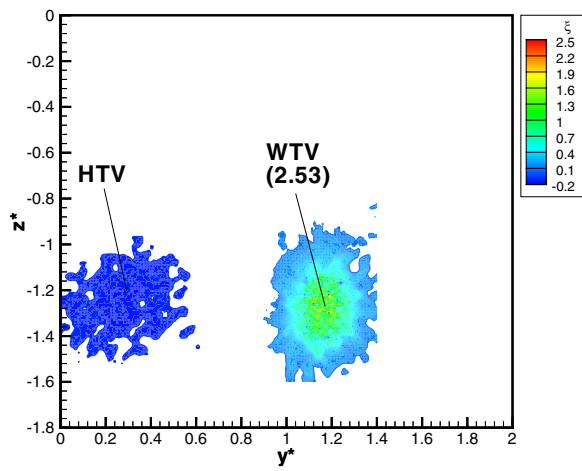


Figure 6: Contour plot of non-dimensional axial vorticity  $\xi$  at  $x^* = 24.0$  and  $Re_c = 8 \times 10^4$

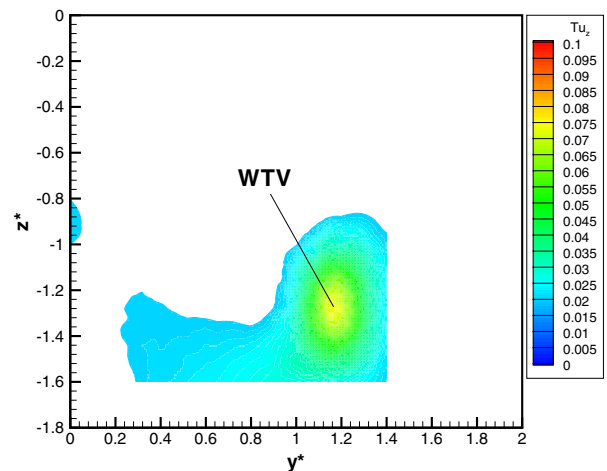


Figure 9: Contour plot of turbulence intensity  $Tu_z$  at  $x^* = 24.0$  and  $Re_c = 8 \times 10^4$

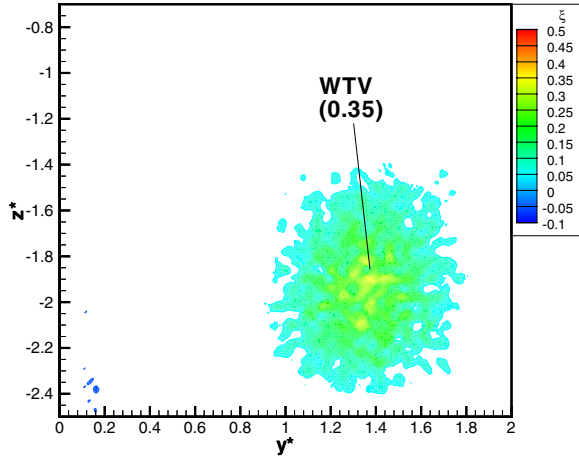


Figure 10: Contour plot of non-dimensional axial vorticity  $\xi$  at  $x^* = 48.0$  and  $Re_c = 8 \times 10^4$

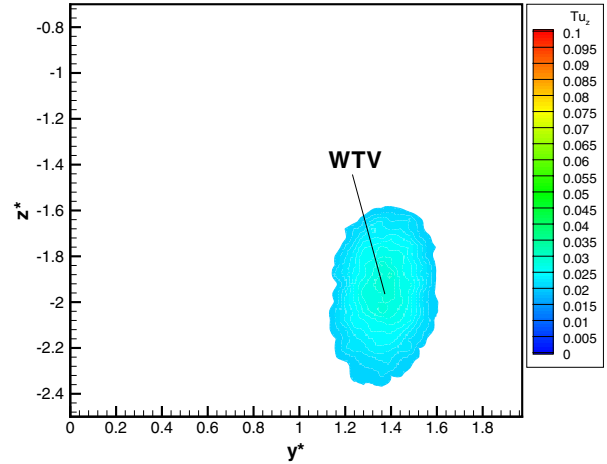


Figure 11: Contour plot of turbulence intensity  $Tu_z$  at  $x^* = 48.0$  and  $Re_c = 8 \times 10^4$

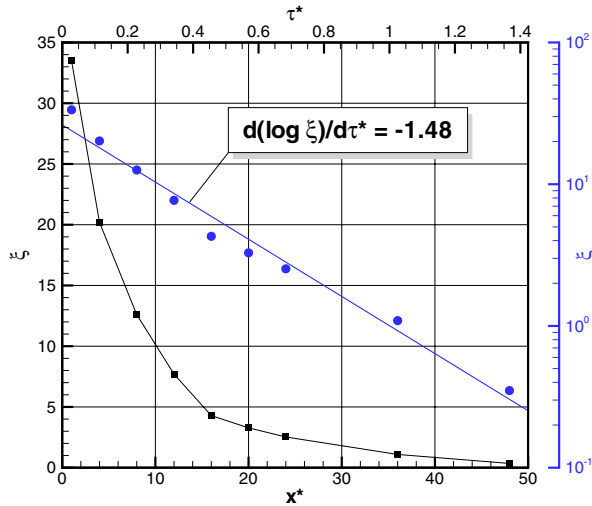


Figure 12: Decay in peak vorticity for the Wing Tip Vortex at  $Re_c = 8 \times 10^4$

centrated vortex to a region of vorticity spots with very low peak levels. The turbulence intensities have decreased further to a level of approx. 3% in the region of the vortex core.

Fig. 12 illustrates the development of the peak vorticity value of the WTV over the downstream distance  $x^*$  and dimensionless time  $\tau^*$ . Between  $\tau^* = 0.05$  and  $\tau^* = 0.5$  there is a rapid decrease in the peak vorticity level with a reduction by an order of magnitude. In this time period the instability mechanism due to the mutual induction of the neighbored counter-rotating vortices is fully developed leading to a rapid distortion of the main vortex. After  $\tau^* = 0.5$  there is a further reduction of peak vorticity showing again an alleviation by nearly a factor of 10. A logarithmic scaling for the  $\xi$ -axis demonstrates a nearly linear trend in the reduction of the peak vorticity level with a gradient of  $d(\log \xi)/d\tau^* = -1.48$ .

Fig. 13 depicts the track of the vortex center in the  $y^*-z^*$ -

$z^*$ -plane. As stated above the WTV moves downward and outward continuously whereas the HTV moves inward and then outward while always travelling downward. The data for the HTV is only available up to  $x^* = 20.0$ . The downward velocity of the WTV decreases as it moves downstream. Note that the last two data points have a  $\Delta x^*$  of 12, whereas the first seven data points have a  $\Delta x^*$  of 4.

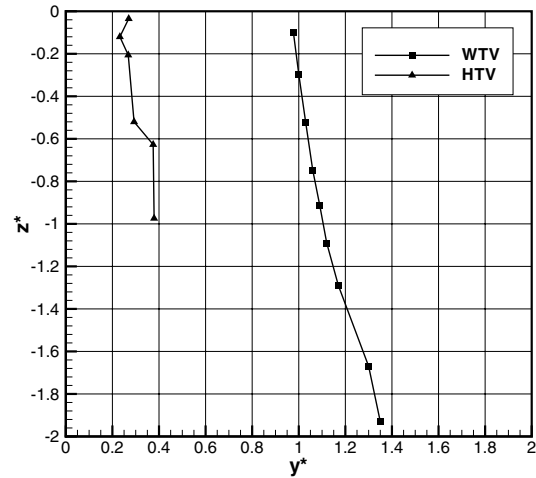


Figure 13: Trajectories of the vortices WTV and HTV in the  $y^*-z^*$ -plane at  $Re_c = 8 \times 10^4$

### 3.3 Spectral analysis

In order to judge the instabilities developing in the vortex system, characteristic spectral peaks are searched indicating that turbulent kinetic energy is channelled into a narrow band due to quasi periodic fluctuations. An overview is given below how the frequency content and related energy overshoots are evaluated with respect to the most dominant

instability mechanisms.

The presence of instability mechanisms propagating along the wake vortex in stream wise direction can lead to a relevant distortion of the vortex, accelerating its dispersion and decay. Usually, long, medium and short wave instabilities occur. The most significant long wave instability for a counter-rotating vortex pair is the Crow<sup>2</sup> instability. This instability is related to the strain effect induced by one vortex of a pair on the other one, and appears as a sinusoidal displacement of the vortex trajectories. The displacement amplitude grows exponentially in time but the amplification factor is low. This kind of instability is ultimately responsible for the wake vortex collapse in the far field. Regarding two vortex pairs Crouch observed an instability mechanism with both symmetric and asymmetric modes, the wavelengths of which are shorter than those of the Crow instability, but large with respect to the effective vortex core size<sup>3</sup>. A Crouch type instability may enhance wake vortex dispersion within  $x/b \approx 30$ .

Wavelengths of Crow and Crouch type instabilities are  $\lambda_{Crow} \approx 8b_0$  and  $\lambda_{Crouch} \approx 1.5d \div 6.0d$ , respectively. In this case two counter-rotating vortex pairs are investigated. The lateral center of circulation is positioned according to Eq. 6, giving  $\tilde{b}_0 = 1.3 b_M$  for the investigated case.

$$(6) \quad \tilde{b}_0 = b_M \left( \frac{1 + R_b R_\Gamma}{1 + R_\Gamma} \right)$$

The typical wavelength for the dominant long wave instability in a counter-rotating vortex pair is described in Eq. 7. Calculating the reduced frequency this leads to Eq. 8 with the initial distance of the main vortices  $b_M$  is approx. equal to the wing span  $b_W$ , see Fig. 13 (Fully developed WTV:  $y^* \cong 1$  for  $x^* \cong 4$ ).

$$(7) \quad \frac{\lambda_{4VS-}}{\tilde{b}_0} \cong 2.5\pi$$

$$(8) \quad k_{dom} = \frac{f_{dom}(b_W/2)}{U_\infty} = \frac{b_W}{2\lambda} = \frac{1}{5\pi} \frac{b_W}{\tilde{b}_0} = 0.049$$

Figs. 14, 15, 16 and 17 illustrate typical power spectral density distributions for the HTV and WTV at the measuring positions  $x^* = 1.0, 12.0, 24.0$  and  $48.0$ . Clearly, distinct peaks are visible around the calculated dominant reduced frequency of  $k_{dom} = 0.049$  indicating the existence of distinct quasi-periodic fluctuations.

### 3.4 Correlation measurements

Correlation measurements have been performed using two hot-wire probes each consisting of three wires. The first probe is at a fixed position  $x_1^*$  within the WTV or

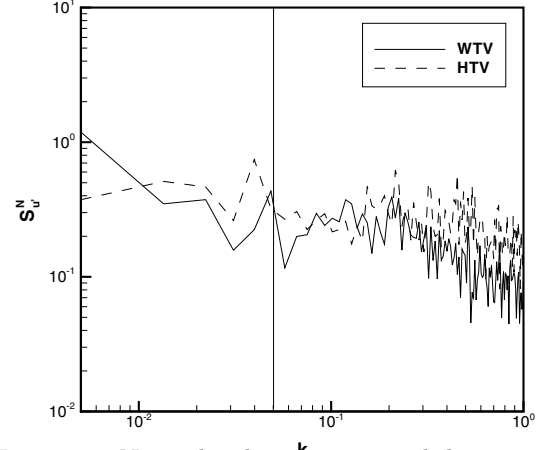


Figure 14: Normalized power spectral densities of the axial velocity fluctuations at  $x^* = 1.0$  and  $Re_c = 8 \times 10^4$

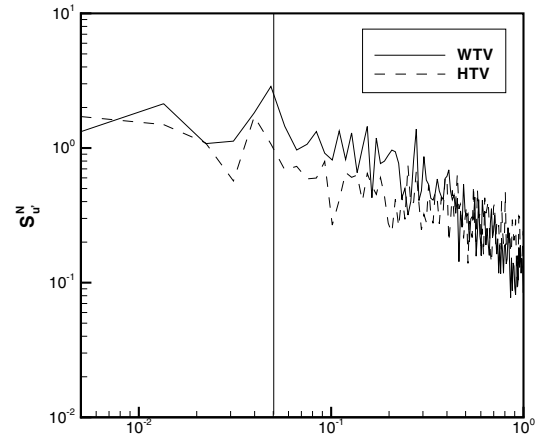


Figure 15: Normalized power spectral densities of the axial velocity fluctuations at  $x^* = 12.0$  and  $Re_c = 8 \times 10^4$

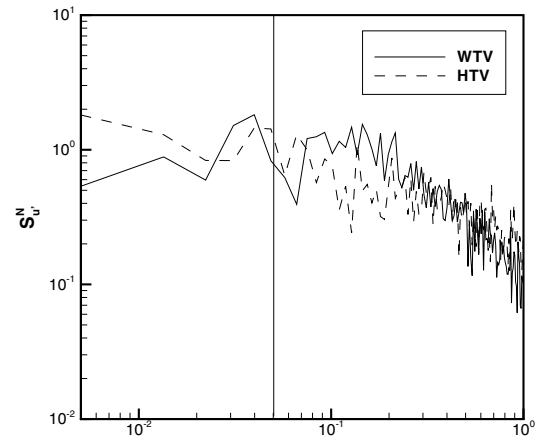


Figure 16: Normalized power spectral densities of the axial velocity fluctuations at  $x^* = 24.0$  and  $Re_c = 8 \times 10^4$

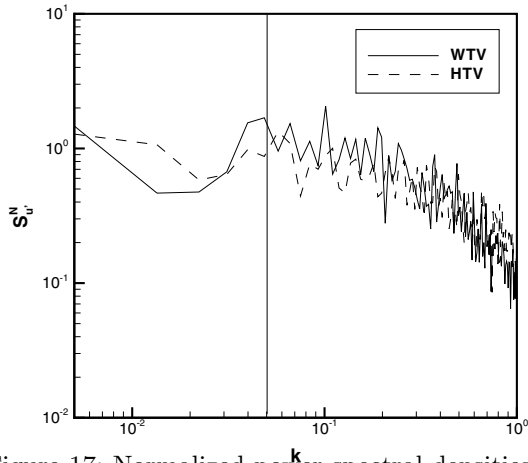


Figure 17: Normalized power spectral densities of the axial velocity fluctuations at  $x^* = 48.0$  and  $Re_c = 8 \times 10^4$

HTV, whereas the second probe is traversed within the same vortex at a position further downstream  $x_2^*$ . The plots shown are cross spectral density distributions of the spanwise velocity fluctuation ( $v'$ ) and have been evaluated using the same parameters as for the power spectral density distributions. The plots illustrate the frequency content in both spectra.

Fig. 18 shows the cross spectral density distributions for the WTV. The vertical line depicts the calculated value for the expected dominant reduced frequency at which distinct peaks should appear. For the WTV a slight shift is noticeable, showing peaks at  $k \approx 0.4$  in all three cases and a significant peak at  $k \approx 0.6$  for the case  $x_1^* = 12.0$  and  $x_2^* = 24.0$ . In the cases with  $x_1^* = 12.0$  energy peaks are also visible at higher harmonics of the dominant reduced frequency. Finding the peaks also with the first probe positioned at  $x_1^* = 12.0$  indicates that the frequency is contained downstream within the vortices.

For the HTV the cross spectral density distributions

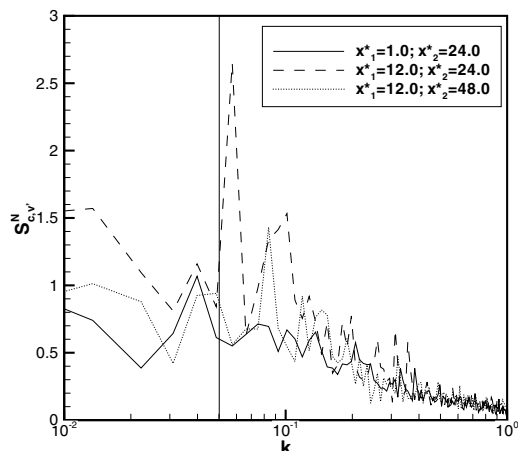


Figure 18: Cross spectral density distributions for the WTV with one probe at  $x_1^*$  and the other one at  $x_2^*$  at  $Re_c = 8 \times 10^4$

are depicted in Fig. 19. Note that the spectral density levels for the HTV are significantly reduced in magnitude in comparison to the WTV. The peaks found match the predicted value very well. Fig. 20 depicts the

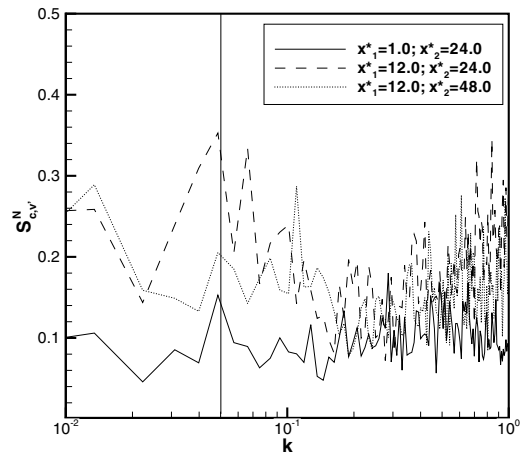


Figure 19: Cross spectral density distributions for the HTV with one probe at  $x_1^*$  and the other one at  $x_2^*$  at  $Re_c = 8 \times 10^4$

spectral results obtained with one probe being within the HTV at  $x^* = 12.0$  and the other one being traversed within the WTV at  $x^* = 12.0$ . At  $k_{dom} \approx 0.049$  a clear peak can be detected substantiating that this frequency is dominant at both measuring positions. Another peak is visible at  $k \approx 2 \cdot k_{dom}$ , illustrating the higher harmonic.

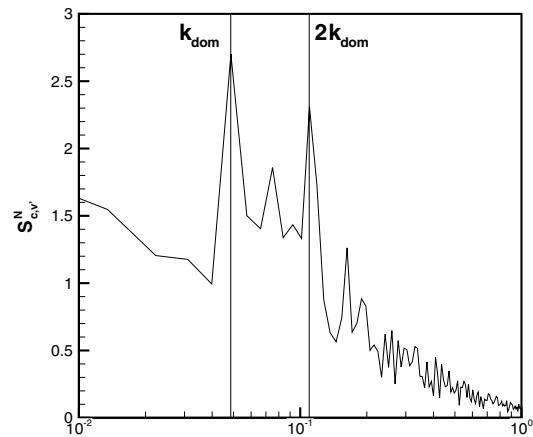


Figure 20: Cross spectral density distributions with both probes at  $x^* = 12.0$  (WTV and HTV) at  $Re_c = 8 \times 10^4$

## 4 CONCLUSION AND OUTLOOK

A comprehensive experimental investigation using the DLR F13 model creating a four-vortex system with counter-rotating neighbored vortices has been conducted. The circulation ratio of tail plane and wing

vortices was set to  $-0.3$  proven by force measurements. The span ratio of tail plane and wing is  $0.3$ . This combination of circulation and span ratio is chosen to create a strong interaction between tail plane and wing vortices resulting in an optimal amplification of the long wave instabilities developing on the wing vortices. The flow fields observed by means of hot-wire anemometry show the wake vortex development up to 48 span dimensions downstream. From the extended near field to the far field the concentrated wing vortex transforms to a vortical structure with a large region of radially distributed vorticity. This structure becomes dominant downstream of 20 span dimensions further expanding strongly in its radial range. Consequently, a rapid decay in axial vorticity is observed for the wing vortex with a gradient  $d(\log \xi)/d\tau^* = -1.48$ . Hence, the peak vorticity level is reduced by one order of magnitude within 30 span dimensions. The movement of the two counter-rotating vortices during this decay is mainly downward and outward. Spectral analysis of the time dependent velocities obtained from the hot-wire tests has been carried out as well. The developing instabilities are attributed to characteristic spectral density peaks. These peaks have been found at a frequency range matching the one predicted by linear stability analysis. The dominant reduced frequency is approx.  $k_{dom} = (1/5\pi)(b_W/\tilde{b}_0)$  with  $b_W$  as wing span and  $\tilde{b}_0$  as the distance between the main vortices centroids. Corresponding findings can be taken from the cross spectral density results obtained by correlation measurements using two hot-wire probes. The wind tunnel results will be compared with data obtained in a towing tank test planned by DLR. Thus, hot-wire results, i.e. turbulence and spectral quantities will be linked with PIV results informing about the spatial wake vortex structure.

## ACKNOWLEDGEMENT

The support of this investigation within the Specific Targeted Research Project "FAR-Wake" of the Sixth Framework Programme of the European Union under Contract No. AST4-CT-2005-012238 is gratefully acknowledged. The authors would like to thank the DLR for providing the wind tunnel models and especially Dr. Robert Konrath, Carl F. v. Carmer and Guido Voss (DLR-AS Göttingen/Braunschweig) for their kind assistance and support.

## REFERENCES

[1] V.J. Rossow: Lift-Generated Vortex Wakes of Subsonic Transport Aircraft. Progress in Aerospace Sciences, Vol. 35, No. 6, pp. 507-560, 1999.  
 [2] K. Hünecke: From Formation to Decay - Extended-time Wake Vortex Characteristics of Transport-type

Aircraft. AIAA Paper 2002-3265, June 2002.

[3] E. Coustols, E. Stumpf, L. Jacquin, F. Moens, H. Vollmers, T. Gerz: "Minimised Wake": A Collaborative Research Programme on Aircraft Wake Vortices. AIAA Paper 2003-0938, Jan. 2003.  
 [4] J.D. Crouch, G. Miller, P.R. Spalart: Active-Control System for Breakup of Airplane Trailing Vortices. AIAA Journal, Vol. 39, No. 12, pp. 2374-2381, 2001.  
 [5] C. Breitsamter, C. Bellastrada, B. Laschka: Investigations on the turbulent wake vortex flow of large transport aircraft. ICAS Proceedings, 23rd International Congress of the Aeronautical Sciences (Toronto, Canada), pp. 382.1-382.13, Sept. 2002.  
 [6] L. Jacquin: FAR-Wake Task 1.2.2: Medium- and Long-wave Cooperative Instabilities, First Year Position Paper. FAR-Wake Technical Report, 2006.  
 [7] S.C. Crow: Stability theory for a pair of trailing vortices. AIAA Journal, 8 (12), pp. 2172-2179, 1970.  
 [8] J.D. Crouch: Instability and transient growth for two trailing vortex pairs. Journal of Fluid Mechanics, Vol. 350, pp. 311-330, 1997.  
 [9] D. Fabre, L. Jacquin: Stability of a four-vortex aircraft wake model. Physics of Fluids 12, pp. 2438-2443, 2000.  
 [10] D. Fabre, L. Jacquin, A. Loof: Optimal perturbations in a four-vortex aircraft wake in counterrotating configuration. Journal of Fluid Mechanics, Vol. 451, pp. 319-328, 2002.  
 [11] C. Donaldson, A. Bilanin: Vortex wakes of conventional aircraft. Technical Report AG-204, AGARD, 1975.  
 [12] R.L. Bristol, J.M. Ortega, P.S. Marcus, Ö Savas: On cooperative instabilities of parallel vortex pairs. Journal of Fluid Mechanics, Vol. 517, pp. 331-358, 2004.  
 [13] Ö. Savas: Experimental investigations on wake vortices and their alleviation. CR-Physique 4-5, 2005.  
 [14] E. Stumpf: Study of Four-Vortex Aircraft Wakes and Layout of Corresponding Aircraft Configurations. Journal of Aircraft, Vol. 42, No. 3, pp. 722-730, May - June 2005.  
 [15] D.A. Durston, S.M. Walker, D.M. Driver, S.C. Smith, Ö. Savas: Wake-Vortex Alleviation Flowfield Studies. Journal of Aircraft, Vol. 42, No. 4, pp. 894-907, July - August 2005.  
 [16] C. Breitsamter: Nachlaufwirbelsysteme großer Transportflugzeuge - Experimentelle Charakterisierung und Beeinflussung. Habilitationsschrift, Technische Universität München, Herbert Utz Verlag (Aerodynamik), Germany (ISBN 3-8316-0713-3), Febr. 2007.